JPE 17-4-10

https://doi.org/10.6113/JPE.2017.17.4.942
ISSN(Print): 1598-2092 / ISSN(Online): 2093-4718

Modified Modular Multilevel Converter with Submodule Voltage Fluctuation Suppression

Xin Huang*, Kai Zhang†, Jingbo Kan*, and Jian Xiong*

†*State Key Laboratory of Advanced Electromagnetic Engineering and Technology, School of Electrical and Electronic Engineering, Huazhong University of Science and Technology, Wuhan, China

Abstract

Modular multilevel converters (MMCs) have been receiving extensive research interest in high/medium-voltage applications due to its modularity, scalability, reliability, high-voltage capability, and excellent harmonic performance. Submodule capacitors are usually rather bulky because they have to withstand fundamental frequency voltage fluctuations. To reduce the capacitance of these capacitors, this study proposes a modified MMC with an active power decoupling circuit within each submodule. The modified submodule contains an auxiliary half bridge, with its capacitor split in two. Also, the midpoints of the half bridge and the split capacitors are connected by an inductor. With this modified submodule, the fundamental frequency voltage fluctuation can be suppressed to a great extent. The second-order voltage fluctuation, which is the second most significant component in submodule voltage fluctuations, is removed by the proper control of the second-order circulating current. Consequently, the submodule capacitance is significantly reduced. The viability and effectiveness of the proposed new MMC are confirmed by the simulation and experimental results. The proposed MMC is best suited for medium-voltage applications where power density is given a high priority.

Key words: Capacitor voltage fluctuation suppression, Circulating current control, MMC

I. INTRODUCTION

At present, an increasing number of high/medium-voltage converters is applied in industry, especially medium-voltage (MV) converters are applied in many applications, such as offshore wind farms, medium voltage DC (MVDC) systems for all-electric ships, and various power quality applications, etc [1]-[4]. Among various high/medium-voltage converters, the neutral-point clamped (NPC) converter, flying capacitor (FC) converter, and cascaded H-bridge (CHB) converter have all received extensive research interests. However, the NPC and FC converters are relatively difficult to extend to more than five levels due to the significantly increased number of clamping diodes or flying capacitors, as well as loss distribution and voltage balance problems. The CHB converter requires a bulky multi-winding transformer to provide a large number of isolated DC sources, which reduces the power density and increases the cost simultaneously [5]. In 2001, Marquart and Lesnicar proposed the modular multilevel converter (MMC) topology [6], which is now considered as the most promising converter topology for high-power and high/medium-voltage applications. The MMC has the advantages of modularity, scalability, reliability, high-voltage capability, and excellent harmonic performance.

However, submodule capacitors of the MMC are usually bulky because they have to withstand fundamental frequency voltage fluctuation. These capacitors usually constitute a major part of the volume and cost of the MMC [7]. Recently, many researchers have been working on reducing the submodule capacitor voltage fluctuation [8]-[17]. In [8]-[15], the fundamental frequency capacitor voltage fluctuation was reduced by introducing the high-frequency circulating current and the common-mode voltage simultaneously to transform the fundamental frequency powers in the submodule capacitors into high frequency ones, thereby achieving low-frequency operation. However, this method is unsuitable for utility frequency scenarios because it nearly doubles the current stress of the power devices and it leaves no room for

Manuscript received May 11, 2016; accepted Apr. 26, 2017
Recommended for publication by Associate Editor Younghoon Cho.
†Corresponding Author: kaizhang@hust.edu.cn
Tel: +86(27)-87543071, Fax: +86(27)-87559303, Huazhong Univ. Sci. Tech.
*State Key Laboratory of Advanced Electromagnetic Engineering and Technology, School of Electrical and Electronic Engineering, Huazhong University of Science and Technology, China

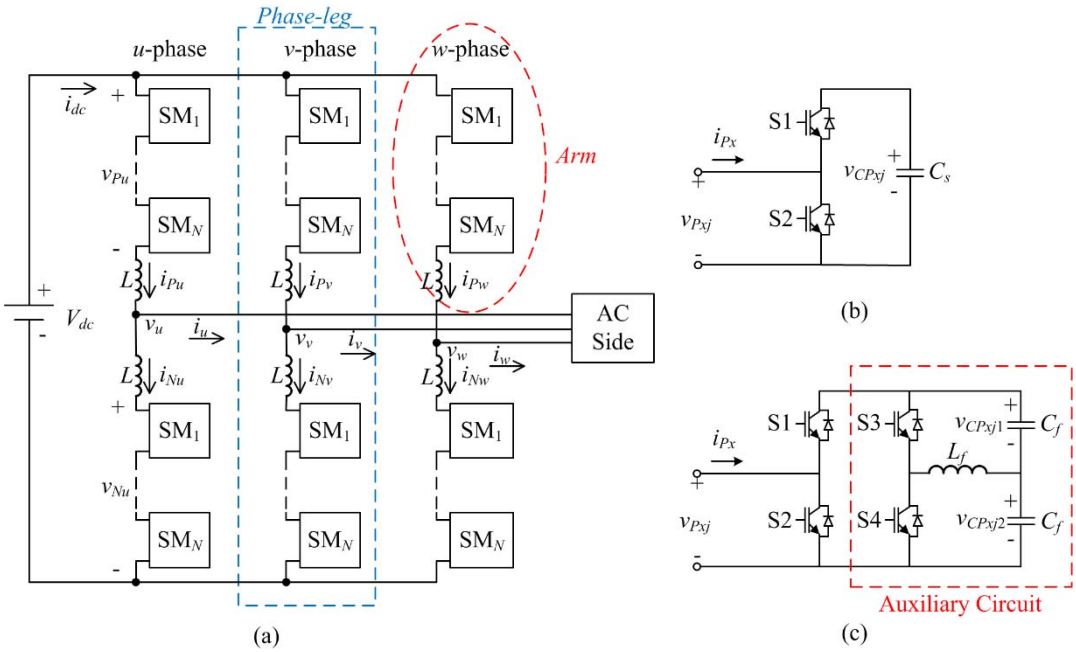

Fig. 1. MMC Topologies. (a) Topology of three-phase MMC. (b) Conventional submodule topology. (c) Proposed submodule with active power decoupling circuit.

the common-mode voltage injection in the modulation index. Reference [16] eliminated the fundamental frequency capacitor voltage fluctuation by adding power channels between the upper and the lower arms. Isolating transformers are necessary in such power channels, which might be tolerable for MV drives but undesirable for high-voltage applications. Reference [17] proposed a modified MMC topology, which can remove fundamental frequency voltage ripples in certain submodules, and a closed-loop control strategy for suppressing the second-order voltage fluctuation. The method is effective in reducing submodule capacitance; however, voltage fluctuations vary among the submodule capacitors, thereby subjecting them to uneven stresses.

This paper investigates the application of the active power decoupling technique [18]-[25] in reducing submodule capacitances. Active power decoupling basically uses an additional power circuit to divert the low-frequency fluctuating power in the main capacitor to an additional energy-storage component (usually another capacitor, which is more efficient than an inductor). The voltage of this additional capacitor does not affect the output voltage/current of the main converter; thus, it can sustain heavy fluctuation, thereby allowing a remarkably small capacitance. The total capacitance (i.e., drastically reduced main capacitance with additional capacitance) with active power decoupling is usually only a fraction of the main capacitance that would be required without active power decoupling. This condition significantly improves power density. Reduced capacitance also allows the application of film capacitors, which improves its reliability and life-time. The inclusion of the additional power circuit (along with the smoothing inductor) definitely occupies some volume and incurs some cost. However, given the ever-improving performances (e.g., higher switching frequency and easier cooling.) and the decreasing price of power devices, volume and cost of the additional circuit are becoming increasingly manageable.

An active power decoupling topology proposed in [25] is employed in this paper. This topology is slightly different from normal ones, such that, it has no additional capacitor; instead, the main capacitor is split in two. This circuit will be used to suppress the most significant, fundamental frequency voltage fluctuation in the submodule capacitors. Then, the remaining second-order voltage fluctuation is removed by a closed-loop control of the second-order circulating current. This way, the submodule voltage fluctuations can be suppressed to a negligible level, and the total capacitance can be significantly reduced.

The remainder of this paper is organized as follows. Section II presents the topology and operating principle of the modified MMC. Section III presents the modeling and control of the fundamental frequency submodule voltage fluctuation suppression. Section IV presents the modeling and control of the second-order submodule voltage fluctuation suppression. The simulation and experimental results are presented in Section V. Section VI concludes this paper.

II. Topology and Operating Principle

A. Modified MMC Topology

The circuit configuration of the modified MMC, which is shown in Fig. 1(a), is similar to that of the conventional MMC except for the auxiliary power decoupling circuits in

the submodules. Figs. 1(b) and 1(c) show the submodules of the conventional MMC and modified MMC, respectively. Each phase leg of the modified MMC consists of two arms, with each arm having N identical submodules and one smoothing inductor. In comparison with the conventional submodule, the modified submodule has an auxiliary half bridge, with its submodule capacitor split in two. The midpoints of the half bridge and the split capacitors are connected by an inductor. As seen from the outside, the submodule has three valid states, namely, on (S1 on and S2 off), off (S1 off and S2 on), and standby (S1 and S2 off) states. The standby state only exists while pre-charging the submodule capacitors.

In Fig. 1, V_{dc} and I_{dc} are the DC-link voltage and current. v_{Px} and v_{Nx} ($x = u$, v, or w) are the summed output voltages of the upper and lower arms. i_{Px} and i_{Nx} are the arm currents. v_x is the AC output voltage of phase x (with respect to the midpoint of the DC-link). v_{CPxj} and v_{CNxj} (j = 1~N) are the individual submodule voltages in the upper and lower arms.

B. Operating Principle at the Converter Level

The auxiliary circuit, as shown in Fig. 1(c), is added to suppress the fundamental frequency fluctuation in the submodule voltage. In comparison with the conventional submodule shown in Fig. 1(b), the only difference (as seen from the main switches S1 and S2) is a smoother DC-side voltage. Thus, the operation of the modified MMC is the same as that of a conventional MMC at the converter level. The derivation and conclusion in this subsection apply to both MMCs.

According to Kirchhoff's voltage law (KVL), the upper- and lower-arm voltages, v_{Px} and v_{Nx}, are

$$\begin{cases} v_{Px} = \frac{1}{2}V_{dc} - v_x - L\frac{di_{Px}}{dt} - Ri_{Px} \\ v_{Nx} = \frac{1}{2}V_{dc} + v_x - L\frac{di_{Nx}}{dt} - Ri_{Nx} \end{cases}, \tag{1}$$

where R represents the equivalent resistance of each arm.

According to Kirchhoff's current law (KCL), output current i_x can be expressed as

$$i_x = i_{Px} - i_{Nx}. \tag{2}$$

Circulating current i_{zx} is defined as

$$i_{zx} = \frac{1}{2}(i_{Px} + i_{Nx}). \tag{3}$$

According to Eqs. (2) and (3), arm currents can be derived as

$$\begin{cases} i_{Px} = i_{zx} + \frac{1}{2}i_x \\ i_{Nx} = i_{zx} - \frac{1}{2}i_x \end{cases}. \tag{4}$$

Substituting Eq. (3) into Eq. (1) yields

$$L\frac{di_{zx}}{dt} + Ri_{zx} = \frac{1}{2}V_{dc} - \frac{1}{2}(v_{Px} + v_{Nx}). \tag{5}$$

According to Eq. (5), the circulating current i_{zx} can be controlled by regulating (v_{Px}+v_{Nx})/2, or the "common-mode" component of the arm voltages. The circulating current i_{zx} mainly contains the DC and second-order components.

To determine the ripple powers flowing into the submodules, which cause submodule capacitor voltage fluctuations, we start with the instantaneous powers of the upper and lower arms in each phase:

$$\begin{cases} p_{Px} = v_{Px}i_{Px} \\ p_{Nx} = v_{Nx}i_{Nx} \end{cases}. \tag{6}$$

In steady state, if the voltage drops on the arm inductors are neglected, then the arm voltages, v_{Px} and v_{Nx}, in Eq. (1) can be rewritten as

$$\begin{cases} v_{Px} = \frac{1}{2}V_{dc} - v_x = \frac{1}{2}V_{dc} - V_x\sin(\omega t + \theta_x) \\ v_{Nx} = \frac{1}{2}V_{dc} + v_x = \frac{1}{2}V_{dc} + V_x\sin(\omega t + \theta_x) \end{cases}, \tag{7}$$

where θ_x is the initial angle of the output voltage of phase x, and V_x is the amplitude of output voltage v_x.

Substituting Eqs. (4) and (7) into Eq. (6), and considering only the DC and second-order components in the circulating current i_{zx}, the arm powers can be expressed as in Eq. (8), where I_{zx_0} is the DC component of the circulating current i_{zx}, I_{zx_2} is the amplitude of the second-order component of the circulating current i_{zx}, θ_{2x} is the initial angle of the second-order component of i_{zx}, and φ is the power factor angle of the load. The DC components of the powers are neglected because they do not exist in a steady state.

$$\begin{cases} p_{Px} = \frac{1}{4}V_{dc}I_x\sin(\omega t + \theta_x - \varphi) - V_xI_{zx\_0}\sin(\omega t + \theta_x) - \frac{1}{2}V_xI_{zx\_2}\cos(\omega t + \theta_{2x} - \theta_x) \\ \quad + \frac{1}{2}V_{dc}I_{zx\_2}\sin(2\omega t + \theta_{2x}) + \frac{1}{4}V_xI_x\cos(2\omega t + 2\theta_x - \varphi) + \frac{1}{2}V_xI_{zx\_2}\cos(3\omega t + \theta_x + \theta_{2x}) \\ p_{Nx} = \frac{1}{4}V_{dc}I_x\sin(\omega t + \theta_x - \varphi) + V_xI_{zx\_0}\sin(\omega t + \theta_x) + \frac{1}{2}V_xI_{zx\_2}\cos(\omega t + \theta_{2x} - \theta_x) \\ \quad + \frac{1}{2}V_{dc}I_{zx\_2}\sin(2\omega t + \theta_{2x}) + \frac{1}{4}V_xI_x\cos(2\omega t + 2\theta_x - \varphi) - \frac{1}{2}V_xI_{zx\_2}\cos(3\omega t + \theta_x + \theta_{2x}) \end{cases} \tag{8}$$

$$p_{Px\_1} = -p_{Nx\_1} = \frac{1}{4}V_{dc}I_x\sin(\omega t + \theta_x - \varphi) - V_xI_{zx\_0}\sin(\omega t + \theta_x) - \frac{1}{2}V_xI_{zx\_2}\cos(\omega t + \theta_{2x} - \theta_x) \tag{9}$$

$$p_{Px\_2} = p_{Nx\_2} = \frac{1}{2}V_{dc}I_{zx\_2}\sin(2\omega t + \theta_{2x}) + \frac{1}{4}V_xI_x\cos(2\omega t + 2\theta_x - \varphi) \tag{10}$$

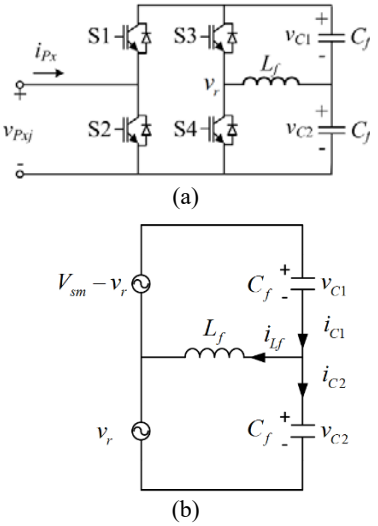

Fig. 2. (a) Topology of proposed submodule. (b) Equivalent circuit model of the power decoupling circuit.

The pulsating arm powers shown in Eq. (8) are supplied by the submodule capacitors. A lower frequency of a power component indicates a larger voltage fluctuation in the submodule capacitors. The fundamental and second-order components of the arm powers are shown in Eqs. (9) and (10).

In a conventional submodule, the pulsating power is supplied by capacitor C_s. The fundamental frequency ripple power is mainly associated with the fundamental voltage fluctuation; thus, the relationship between ripple power and fundamental frequency voltage fluctuation can be expressed as follows:

$$\frac{p_{Px\_1}}{N} = C_s \frac{dv_{1st}}{dt} V_{sm}, \tag{11}$$

where V_{sm} is the DC component of the submodule voltage, and v_{1st} is the instantaneous value of the fundamental component in the submodule voltage. To reduce the voltage fluctuation, the only alternative is to increase submodule capacitance C_s. Given the low frequencies of the ripple powers, C_s has to be significantly large.

In this paper, the fundamental frequency voltage fluctuation is eliminated by the auxiliary power decoupling circuit added to each submodule. The second-order voltage fluctuation is eliminated by properly controlling the circulating current. With this process, the total submodule capacitance can be significantly reduced. The next two sections address the two issues respectively.

III. Operating Principle, Modeling, and Control of the Auxiliary Power Decoupling Circuit

The proposed submodule topology (taking the j-th one in the upper arm of phase x for example) is redrawn in Fig. 2(a), with the capacitor voltages denoted with v_{C1} and v_{C2} for simpler subscripts. Power decoupling circuit is basically controlling the voltages of the two split capacitors to be the sinusoids with opposite phases, together with the DC offsets [25]. The exact voltage references for the two capacitors are the resulted total capacitor power (minus the inductor power), which is equal to p_{Px_1}/N. Simultaneously, no fundamental frequency fluctuation exists in the submodule voltage $v_{C1}+v_{C2}$ because the alternating parts of the two capacitor voltages always cancel each other.

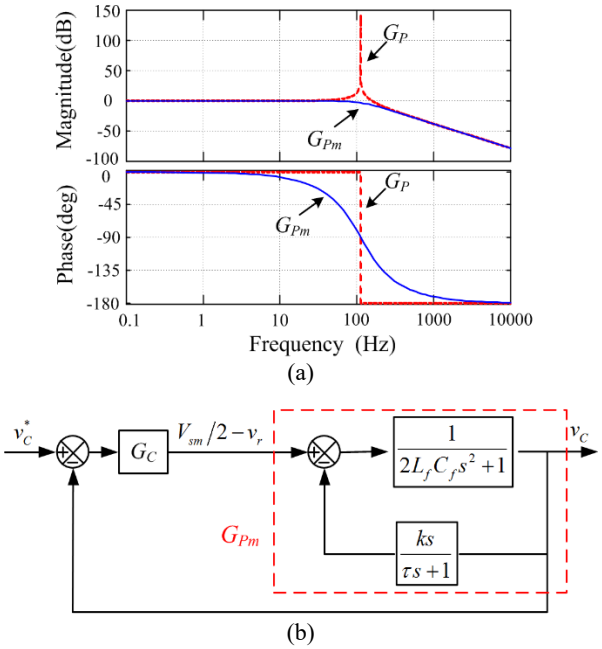

Fig. 3. (a) Effect of active damping. (b) Overall control block diagram of the power decoupling circuit.

A. Calculation of Capacitor Voltage References

Suppose that the form of the voltage references of the two split capacitors are as follows:

$$\begin{cases} v_{C1} = \frac{1}{2}V_{sm} + v_C = \frac{1}{2}V_{sm} + V_C \sin(\omega_C t + \theta_C) \\ v_{C2} = \frac{1}{2}V_{sm} - v_C = \frac{1}{2}V_{sm} - V_C \sin(\omega_C t + \theta_C) \end{cases}, \tag{12}$$

where $V_{sm} = v_{C1}+v_{C2}$ is the expected ripple-free submodule voltage (half of which is considered as the common DC offset in this study), ω_C is the angular frequency of the capacitor voltage, θ_C is the initial angle of the capacitor voltage, and V_C is the amplitude of the sinusoidal component.

The capacitor currents are thus

$$\begin{cases} i_{C1} = C_f \frac{dv_{C1}}{dt} = \omega_C C_f V_C \cos(\omega_C t + \theta_C) \\ i_{C2} = C_f \frac{dv_{C2}}{dt} = -\omega_C C_f V_c \cos(\omega_C t + \theta_C) \end{cases}. \tag{13}$$

With Eqs. (12) and (13), the total power provided by the two capacitors can be derived as

$$p_{aC} = v_{C1}i_{C1} + v_{C2}i_{C2} = \omega_C C_f V_C^2 \sin(2\omega_C t + 2\theta_C). \tag{14}$$

According to KCL, the inductor current can be derived as

TABLE I
EXPERIMENTAL PARAMETERS OF THE PROPOSED MMC

Items	Value
DC-link voltage, V_{dc}	500 V
Arm inductance, L	4.6 mH
No. of submodules per arm, N	2
Submodule voltage, V_{sm}	250 V
Submodule capacitance, C_f	220 μF
Filter inductance, L_f	4 mH
Switching frequency	2 kHz
Modulation index, M	0.6

$$i_{Lf} = i_{C1} - i_{C2} . \quad (15)$$

Thus, the power of the smoothing inductor can be expressed as

$$p_{aL} = L_f \frac{di_{Lf}}{dt} i_{Lf} = -2\omega_C L_f (\omega_C C_f V_C)^2 \sin(2\omega_C t + 2\theta_C) . \quad (16)$$

Hence, the total power provided by the auxiliary circuit is

$$\begin{aligned} p_a &= p_{aC} + p_{aL} \\ &= [\omega_C C_f V_C^2 - 2\omega_C L_f (\omega_C C_f V_C)^2] \sin(2\omega_C t + 2\theta_C) \end{aligned} . \quad (17)$$

N times of p_a should be equal to the fundamental component of the arm power derived in Eq. (9). The submodule here is assumed to be one from the upper arm of phase x; thus,

$$N p_a = p_{Px\_1} . \quad (18)$$

With Eq. (18), V_C, ω_C, and θ_C in Eq. (12) can be solved as follows:

$$\begin{cases} \omega_C = \frac{1}{2}\omega \\ \theta_C = \frac{1}{2}\arctan\frac{A}{B} \\ V_C = \sqrt{\frac{\sqrt{A^2 + B^2}}{\omega_C C_f - 2\omega_C L_f (\omega_C C_f)^2}} \end{cases} , \quad (19)$$

where

$$A = \frac{1}{N}[\frac{1}{4} V_{dc} I_x \sin(\theta_x - \varphi) - V_x I_{zx\_0} \sin\theta_x - \frac{1}{2} V_x I_{zx\_2} \sin(\theta_{2x} - \theta_x)] ,$$

and

$$B = \frac{1}{N}[\frac{1}{4} V_{dc} I_x \cos(\theta_x - \varphi) - V_x I_{zx\_0} \cos\theta_x + \frac{1}{2} V_x I_{zx\_2} \sin(\theta_{2x} - \theta_x)]$$

. If the submodule is from a lower arm, then $\theta_C = \frac{1}{2}\arctan\frac{A}{B} + \frac{\pi}{2}$.

B. Modeling of the Power Decoupling Circuit

It is the task of the auxiliary half bridge (S3 and S4) to conduct the voltage tracking control of the two capacitors. By representing the actual (PWM style) output voltage of the half bridge with its state–space averaged value v_r, the equivalent circuit model (or the state–space averaged model) of the power decoupling circuit is shown in Fig. 2(b). v_r also serves as the modulation signal of S4, whereas $V_{sm}-v_r$ is the modulation signal of S3. The relationship from v_r to the capacitor voltages (specifically, their alternating parts) should be determined to design the tracking control system for the capacitor voltages properly.

According to KVL and neglecting the inductor's resistance, two voltage equations can be established:

$$\begin{cases} v_r - V_{sm} + v_{C1} + L_f \frac{di_{Lf}}{dt} = 0 \\ -v_r - L_f \frac{di_{Lf}}{dt} + v_{C2} = 0 \end{cases} . \quad (20)$$

By subtracting the two equations of Eq. (12), the sinusoidal (or the differential) component of the capacitor voltages can be expressed as follows:

$$v_C = \frac{v_{C1} - v_{C2}}{2} . \quad (21)$$

Eqs. (20) and (21) yield

$$v_r - \frac{V_{sm}}{2} + v_C + L_f \frac{di_{Lf}}{dt} = 0 . \quad (22)$$

According to Eqs. (13), (15), and (21), the inductor current can be rewritten as

$$i_{Lf} = 2C_f \frac{dv_C}{dt} . \quad (23)$$

Substituting Eq. (23) into Eq. (22) yields

$$2L_f C_f \frac{d^2 v_C}{dt^2} + v_C = \frac{V_{sm}}{2} - v_r . \quad (24)$$

The right side of Eq. (24) is actually the alternating part of the modulation signal for S3. Hence, finding the transfer function between $V_{sm}/2-v_r$ and v_C seems convenient and useful, which can be expressed as follows:

$$G_P = \frac{v_C}{V_{sm}/2 - v_r} = \frac{1}{2L_f C_f s^2 + 1} . \quad (25)$$

C. Control of the Power Decoupling Circuit

The controller design of the power decoupling circuit is conducted based on the parameters listed in Table I. The Bode plot of plant G_P is shown as the red dotted line in Fig. 3(a). A high resonance peak exists at the LC resonant frequency, $\omega_r = 1/\sqrt{2L_f C_f}$, which negatively affects system stability. In this study, active damping by means of capacitor voltage feedback (See Fig. 3(b), which shows the overall control system) is applied to eliminate the resonance peak. Shown in Fig. 3(a) with blue solid line is the Bode plot of the modified plant G_{Pm}. The transfer function of G_{Pm} is

$$G_{Pm} = \frac{v_C}{V_{sm}/2 - v_r} = \frac{1}{2L_f C_f s^2 + \frac{ks}{\tau s + 1} + 1} , \quad (26)$$

where k is determined by the expected damping effect, and τ is a small time constant.

A proportional additional quasi-resonant controller is adopted as the voltage controller to track the reference v_C^*, which is a 25-Hz sinusoid. The transfer function of the proportional and quasi-resonant controller is expressed as

$$G_C = K_p + \frac{2K_r\omega_b s}{s^2 + 2\omega_b s + \omega_a^2}, \quad (27)$$

where ω_a = 25 Hz is the resonance frequency of the quasi-resonant controller, and ω_b is the bandwidth of the quasi-resonant controller [26].

As shown in Fig. 3(b), the output of G_C is $V_{sm}/2-v_r$. Thus, the modulating signals for S3 and S4 (i.e., $V_{sm}-v_r$ and v_r, respectively) can be readily constructed.

D. Parameter Design of the Power Decoupling Circuit

Inductance L_f should be as small as possible, considering its weight/cost and negative contribution in supplying reactive power (See Eq. (17)). However, a considerably small value of L_f may bring a high switching ripple current, which raises the current stress of S3 and S4. The relationship between L_f and the peak-to-peak ripple current i_{Lf_pp} is expressed as

$$i_{Lf\_pp} = \frac{V_{sm}T_s}{4L_f}. \quad (28)$$

Therefore, L_f can be determined given i_{Lf_pp}.

C_f can become smaller by applying a higher alternating component V_C across the capacitors. However, V_C should not exceed its DC offset $V_{sm}/2$, that is,

$$V_C = \sqrt{\frac{\sqrt{A^2+B^2}}{\omega_C C_f - 2\omega_C L_f(\omega_C C_f)^2}} \le \frac{1}{2}V_{sm}. \quad (29)$$

By solving Eq. (29), the constraints on C_f can be derived as

$$-C + \frac{1}{4\omega_C^2 L_f} \le C_f \le C + \frac{1}{4\omega_C^2 L_f}, \quad (30)$$

where $C = \frac{\sqrt{V_{sm}^2 - 32\omega_c L_f\sqrt{A^2+B^2}}}{4\omega_C^2 L_f V_{sm}}$, in which the lower limit is more useful. The reason why there is an upper limit is that a considerably large capacitance denotes a remarkably high current flowing through the inductor L_f, which causes the counter-productive inductor power to soar; this condition also results in a larger V_C, (i.e., a greater capacitor power to keep p_a unchanged).

IV. Elimination of Second-order Fluctuation in Submodule Voltage

With the fundamental frequency voltage fluctuation eliminated with the auxiliary power decoupling circuit, the second-order pulsating component becomes the most significant. To solve this problem, a closed-loop control strategy similar to [17] is adopted, with a more in-depth analysis. The second-order ripple power needed by the MMC load basically has to be supplied (or balanced) by the submodule capacitors and the DC source of the MMC. The amount of contribution from the DC source is reflected by the second-order component of the circulating current i_{zx}. The DC source can supply all the second-order ripple power by properly controlling the second-order component of the circulating current i_{zx}, whereas the submodules can no longer supply any; thus, the second-order fluctuation in the submodule voltages is eliminated.

The second-order ripple power of the submodule is assumed to be solely associated with the second-order ripple voltage in the submodule. This assumption is valid because although the second-order power can also be generated from the fundamental frequency voltage, which has been the reason for the power decoupling circuit, the latter has been effectively removed from the submodule voltage by the power decoupling circuit.

The proposed control system consists of a current inner loop for tracking control of the second-order circulating current and a voltage outer loop for suppressing the second-order fluctuation in the submodule voltage.

By using the Laplace transform of Eq. (5), the plant model of the circulating current inner loop can be derived as

$$G_{Pi} = \frac{i_{zx}}{\frac{1}{2}V_{dc} - \frac{1}{2}(v_{Px}+v_{Nx})} = \frac{i_{zx}}{v_{zx}} = \frac{1}{sL+R}. \quad (31)$$

To trace the circulating current with the second-order component, a proportional-integral and quasi-resonant controller is adopted with ω_a = 100 Hz. The block diagram of the circulating current control is shown in Fig. 4 (i.e., the dashed line enclosed area). Each phase of the MMC needs one of such control system.

The reference of the second-order circulating current comes from the outer loop controller, which attempts to regulate the second-order component of the submodule voltage toward zero. Generally, even-order (mainly the second order) submodule voltage fluctuations for the upper and lower arms are in each phase, whereas the odd-order fluctuations are opposite in each phase [28]. Therefore, the total submodule voltage of each phase is approximately the summed second-order voltages, together with the total DC offset $2V_{dc}$. If the $2N$ submodule voltages are well balanced, then the average submodule voltage (v_{sm}) equals the second-order voltage fluctuation (v_{2nd}) plus the DC offset V_{dc}/N in each submodule, that is,

$$\begin{aligned} v_{sm} &= \frac{1}{2N}\left(\sum_{j=1}^{N}(v_{CPxj1}+v_{CPxj2}) + \sum_{j=1}^{N}(v_{CNxj1}+v_{CNxj2})\right) \\ &= v_{2nd} + \frac{V_{dc}}{N} \end{aligned}. \quad (32)$$

To determine the plant model for the outer loop, the relationship among the instantaneous powers of the DC source, the $2N$ submodules, and the load should be initially investigated. At any given moment, the three powers should be balanced, that is,

$$V_{dc}i_{zx} = 2Nv_{sm}C_s\frac{dv_{sm}}{dt} + p_x, \quad (33)$$

where $C_s = C_f/2$ is the submodule equivalent capacitance, and p_x is the phase-x load power. Assume the first v_{sm} in Eq. (33)

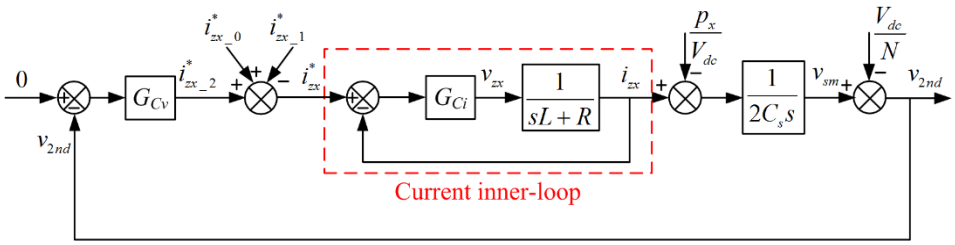

Fig. 4. Suppression control system of second-order ripple voltage.

TABLE II
SIMULATION PARAMETERS OF THE PROPOSED MMC

Items	Value
DC-link voltage, V_{dc}	8000 V
Rated power, P	300 kW
Arm inductance, L	1.5 mH
No. of submodules per arm, N	4
Submodule voltage, V_{sm}	2000 V
Submodule capacitance, C_f	600 μF
Filter inductance, L_f	4 mH
Switching frequency	2 kHz

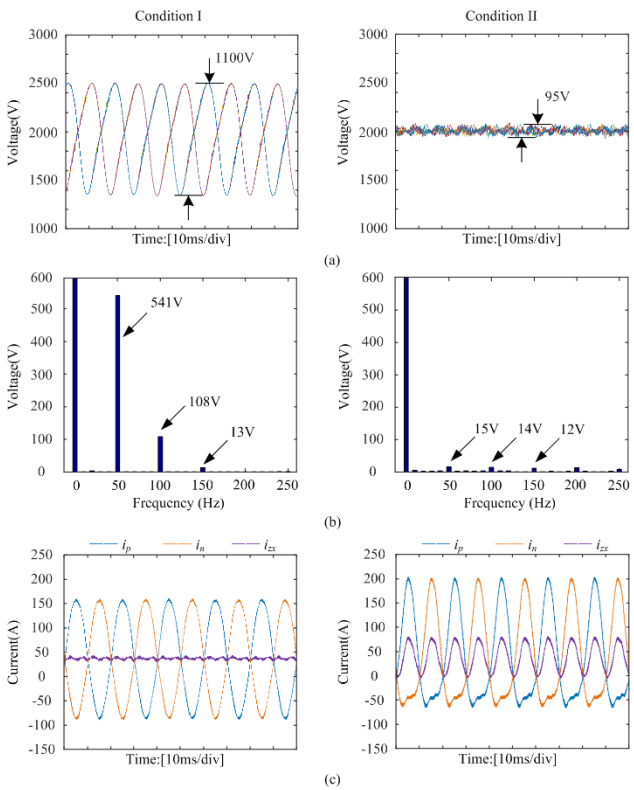

Fig. 5. Simulation waveforms of the MMC operating in Conditions I and II. (a) Submodule voltages. (b) FFT analysis of one submodule voltage. (c) The arm currents and circulating current.

to be approximately V_{dc}/N for ease of analysis. Eq. (33) can be rewritten as

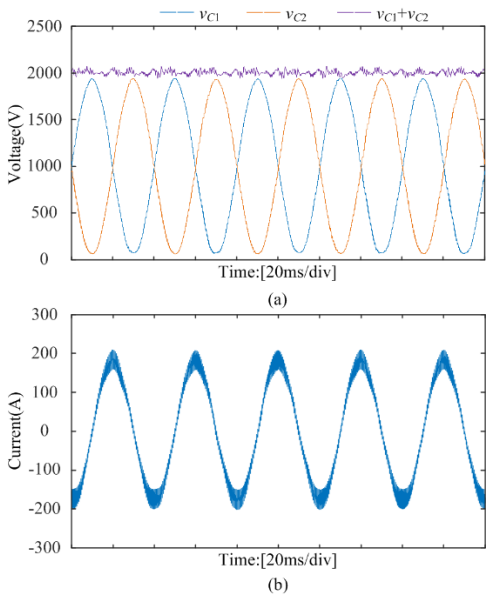

Fig. 6. Simulated voltage/current waveforms within one submodule. (a) Simulated capacitor voltages and submodule voltage. (b) Simulated current of inductor L_f (i_{Lf}).

$$V_{dc} i_{zx} = 2V_{dc} C_s \frac{dv_{sm}}{dt} + p_x \,. \tag{34}$$

By taking the Laplace transform of Eq. (34) and treating the load ripple power p_x as an extraneous disturbance, the transfer function from i_{zx} to v_{sm} can be obtained as

$$G_{Pv} = \frac{v_{sm}}{i_{zx}} = \frac{1}{2C_s s} \,. \tag{35}$$

In a steady state, the power terms in Eq. (34) contain DC and the second-order components. In cases where only the second-order ripple power is concerned, Eq. (34) can be rewritten as

$$V_{dc} i_{zx\_2} = 2V_{dc} C_s \frac{dv_{2nd}}{dt} + p_{x\_2} \,, \tag{36}$$

where i_{zx_2} is the second-order component of i_{zx}, and p_{x_2} is the phase-x second-order ripple power of the load. The suppression control aims to control i_{zx_2}, such that the DC source provides all the second-order ripple power needed by the load (i.e., $V_{dc}\, i_{zx\_2} = p_{x\_2}$).

A proportional and quasi-resonant controller is adopted

$$v_{2nd} = \frac{1}{2N}\left(\sum_{j=1}^{N}(v_{CPxj1} + v_{CPxj2}) + \sum_{j=1}^{N}(v_{CNxj1} + v_{CNxj2})\right) - \frac{V_{dc}}{N} = v_{sm} - \frac{V_{dc}}{N} \tag{37}$$

TABLE III
CURRENTS OF ARMS AND POWER DECOUPLING CIRCUITS

Items	Value
I_{Px_rms}	179 A
$\lvert I_{Px}\rvert_{avg}$	165 A
I_{Lf_rms}	127 A
$\lvert I_{Lf}\rvert_{avg}$	114 A

again for the outer-loop. The entire suppression control system of the second-order submodule ripple voltage is shown in Fig. 4. The reference of the second-order fluctuation is zero; and the feedback of the second-order fluctuation is provided by rewriting Eq. (32) as Eq. (37).

The actual circulating current reference i_{zx}^* has to include its DC component $i_{zx\_0}^*$ and its fundamental component $i_{zx\_1}^*$, which come from total energy control and differential energy control [27] of the submodules, respectively. These signals are denoted in the figure; however, the details of the related control systems are not discussed here because as part of the converter-level control, they are not much different here.

V. SIMULATION AND EXPERIMENTAL RESULTS

A. Simulation Results

To verify the proposed method, a simulation model of a single-phase MMC inverter is established in MATLAB/Simulink. The parameters are listed in Table II. The load is a resistor.

First, two operational conditions are compared to demonstrate the performance of the proposed method. In Condition I, the MMC operates in a conventional condition (i.e., S3 and S4, which are the inactive and suppression control for the second-order ripple voltage, are turned off). In Condition II, the MMC operates with the proposed power decoupling circuit and suppression control of second-order ripple voltage. The simulation results are shown in Fig. 5. From the figure, the two most significant harmonic components, namely, the fundamental and second-order components, have been virtually eliminated using the proposed method. As a result, the peak-to-peak fluctuation of the submodule voltage is reduced from 1100 V to 95 V. For a conventional submodule (Fig. 1(b)), a 3.5-mF capacitance is required to obtain the same suppression effect.

With the suppression control of the second-order ripple voltage, the second-order ripple power is transferred from the submodules to the DC source. Therefore, a second-order component exists in the circulating current, and both arm currents are slightly shifted upward.

Fig. 6(a) and 6(b) shows the capacitor voltages, the submodule voltage, and the inductor current within one submodule of the modified MMC in simulations. The ripple

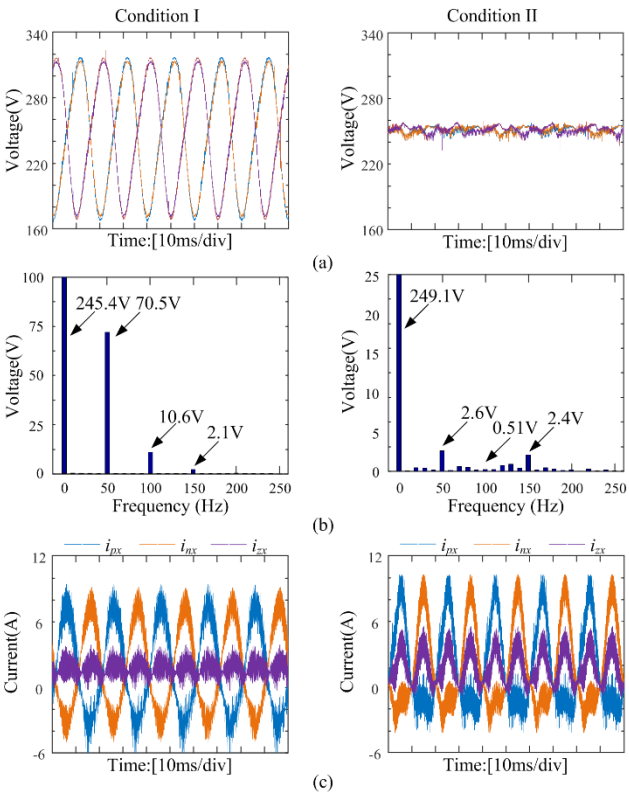

Fig. 7. Experimental waveforms of the MMC operating in Conditions I and II. (a) Submodule voltages. (b) FFT analysis of one submodule voltage. (c) Arm currents and circulating current.

current can be further reduced if a high switching frequency is adopted. The fundamental component of the inductor current is approximately the same as the arm current, which indicates a same level of current stress for S1/S2 and S3/S4.

B. Power Loss Comparison

Introducing active circuitry into the submodule will inevitably affect the efficiency. To assess the effect, the power losses associated with IGBTs and diodes of conventional MMC and the proposed MMC are compared. The loss calculation method in Reference [29] is adopted.

IGBT and diode power losses can be classified as conduction, switching, and blocking losses (usually negligible). The simplified model of IGBT with a voltage source (v_{CE0}), which represents on-state zero-current collector-emitter voltage, and a series-connected collector-emitter on-state resistance (r_C) are used to calculate conduction losses. Similarly, the same approximation can be used for the anti-parallel diode. Hence, the instantaneous value of the conduction loss for the IGBT (p_{CT}) and the diode (p_{CD}) can be expressed as

$$\begin{cases} p_{CT} = v_{CE0} i_C + r_C i_C^2 \\ p_{CD} = v_{D0} i_D + r_D i_D^2 \end{cases}. \tag{38}$$

The half-bridge S1/S2 in Fig. 1(c) is considered as an example. When $i_{Px} > 0$, the average conduction loss in one fundamental period ($1/f_1$) is

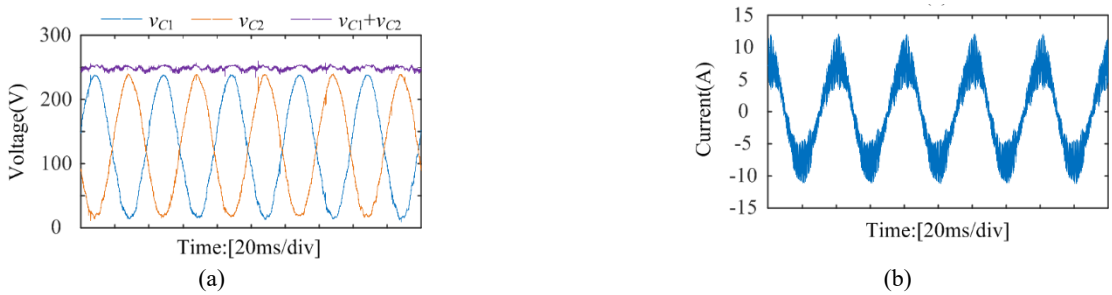

(a) (b)

Fig. 8. Experimental voltage/current waveforms within one submodule. (a) Experimental capacitor voltages and submodule voltage. (b) Experimental current of inductor L_f (i_{Lf}).

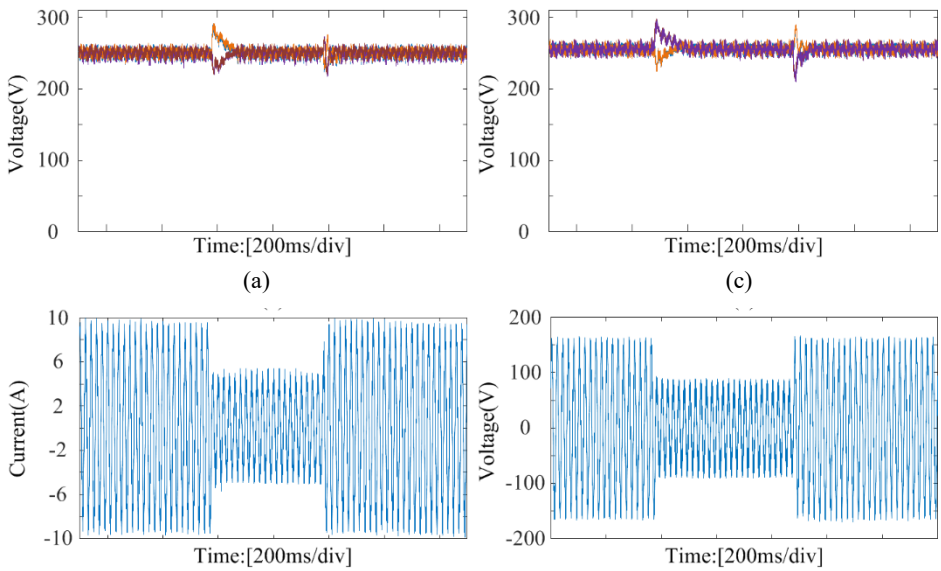

(a) (c)

(b) (d)

Fig. 9. Experimental waveforms during transient processes. (a) Submodule voltages with 50% step-down and step-up of load current. (b) Output current with 50% step-down and step-up of load current. (c) Submodule voltages with 50% step-down and step-up of modulation index. (d) Output voltage with 50% step-down and step-up of modulation index.

$$P_{C1} = f_1\int_t^{t+1/f_1}\left(v_{D0}i_{Px} + r_D i_{Px}^2\right)S(\tau)d\tau + f_1\int_t^{t+1/f_1}\left(v_{CE0}i_{Px} + r_C i_{Px}^2\right)\left[1-S(\tau)\right]d\tau, \quad (39)$$

where $S(t)$ is the switching function and is defined as follows:
$S(t) = 1$: S1 on and S2 off, submodule capacitor inserted;
$S(t) = 0$: S1 off and S2 on, submodule capacitor bypassed.

Similarly, when $i_{Px} < 0$, the average conduction loss is

$$P_{C2} = f_1\int_t^{t+1/f_1}\left[v_{CE0}\left(-i_{Px}\right) + r_C i_{Px}^2\right]S(\tau)d\tau + f_1\int_t^{t+1/f_1}\left[v_{D0}\left(-i_{Px}\right) + r_D i_{Px}^2\right]\left[1-S(\tau)\right]d\tau. \quad (40)$$

Assume the time interval, in which $i_{Px} > 0$ to be T_P, and Eqs. (39) and (40) are combined. Then, the average conduction loss in one fundamental period ($1/f_1$) can be derived as

$$P_C = \frac{T_P}{1/f_1}P_{C1} + \left(1-\frac{T_P}{1/f_1}\right)P_{C2} = \frac{T_P}{1/f_1}\left(v_{CE0}\left|I_{Px}\right|_{avg} + r_C I_{Px\_rms}^2\right) + \left(1-\frac{T_P}{1/f_1}\right)\left(v_{D0}\left|I_{Px}\right|_{avg} + r_D I_{Px\_rms}^2\right), \quad (41)$$

where $|I_{Px}|_{avg}$ is the average value of absolute arm current, and I_{Px_rms} is the root mean square value of the arm current.

On the basis of the specific curves that depict the various switching energy losses against the current, which can be found from power device datasheets, switching loss (P_{sw}) is approximated as

$$P_{sw} = f_s\left(E_{onT} + E_{offT} + E_{rec}\right), \quad (42)$$

where E_{onT} and E_{offT} are the switch-on and switch-off energy losses of IGBT, respectively; and E_{rec} is the reverse-recovery energy loss of diode.

Infineon FD400R33KL2C IGBT module is selected for the simulation model. The parameters for power loss calculation can be read from the IGBT datasheet [30]. The currents of the arms and power decoupling circuits are listed in Table III. According to Eqs. (41) and (42), the power losses of the conventional MMC and the proposed MMC can be estimated. The efficiency of the conventional MMC is 97.91%, and the efficiency of the proposed MMC is 96.06%. The decrease in efficiency is mild considering the significant reduction of submodule capacitance.

C. Experimental Results

Experiments are conducted on a single-phase MMC test setup. The parameters are as listed in Table I. The load is a resistor. The control system is implemented using a TMS320F2812 DSP from Texas Instruments. An EP1C12Q240I7 FPGA performs the pulse–width modulation.

Experimental comparisons of submodule voltages, arm currents, and circulating currents with Conditions I and II (as described in Section 5-A) are presented in Fig. 7. Similar to the simulation results in Fig. 5, the fundamental and second-order fluctuation voltages are effectively suppressed, with the peak-to-peak fluctuation of the submodule voltage decrease from 148 V to 18 V.

Figs. 8(a) and 8(b) shows the capacitor voltages, the submodule voltage, and inductor current within one submodule of the modified MMC in experiments. The results are similar to the simulation results presented in Figs. 6(a) and 6(b).

Experimental waveforms during transient processes are presented in Fig. 9. Two types of transients are investigated, namely, the load step changes and the step changes of the modulation index, which determines the output voltage. As shown in Fig. 9, the submodule voltage that dips/swells during transients are well within 20% of the rated voltage. No visible low-frequency fluctuations in the submodule voltages are observed during the transients. Moreover, the submodule voltages can converge to their rated values within five line cycles.

VI. Conclusions

The submodule capacitors in an MMC are usually bulky to withstand fundamental frequency and second-order voltage fluctuations. The capacitors therefore constitute a major part in the cost and volume of an MMC. In this study, a power decoupling circuit is added to the conventional submodule topology to eliminate the fundamental frequency voltage fluctuation at the submodule level. A circulating current-based closed-loop control system is then employed to eliminate the remaining second-order fluctuation. Simulations and experiments prove that the proposed method works well, and the two major submodule voltage fluctuation components are suppressed effectively. The submodule capacitance can be roughly reduced by three-fold. Although the modified submodule uses two more active devices and a smoothing inductor, the total volume and cost of the MMC system may still be reduced, considering the fact that the new generation of power devices (and their driving circuits) consistently perform well and at a lower cost and convenient size. The smoothing inductor can also be reduced with high switching frequencies. This study provides a probable solution for MV applications where power density is given a high priority.

Acknowledgment

This work was supported by the National Natural Science Foundation of China (Project No.51477063).

References

[1] H. Liu, K. Ma, Z. Qin, P. C. Loh, and F. Blaabjerg, “Lifetime estimation of MMC for offshore wind power HVDC application,” *IEEE J. Emerg. Sel. Topics Power Electron.*, Vol. 4, No. 2, pp. 504-511, Jun. 2016.

[2] Y. Chen, Z. Li, S. Zhao, X. Wei, and Y. Kang, “Design and implementation of a modular multilevel converter (MMC) wtih hierarchical redundancy ability for electric ship MVDC system,” *IEEE J. Emerg. Sel. Topics Power Electron.*, Vol. 5, No. 1, pp. 189-202, Mar. 2017.

[3] S. Du and J. Liu, “A study on DC voltage control for chopper-cell-based modular multilevel converters in D-STATCOM application,” *IEEE Trans. Power Del.*, Vol. 28, No. 4, pp. 2030-2038, Oct. 2013.

[4] Z. Shu, M. Liu, L. Zhao, S. Song, Q. Zhou, and X. He, “Predictive harmonic control and its optimal digital implementation for MMC-based active power filter,” *IEEE Trans. Ind. Electron.*, Vol. 63, No. 8, pp.Aug. 2016.

[5] S. Kouro, M. Malinowski, K. Gopakumar, J. Pou, L. G. Franquelo, B. Wu, J. Rodriguez, M. A. Perez, and J. I. Leon, “Recent advances and industrial applications of multilevel converters,” *IEEE Trans. Ind. Electron.*, Vol. 57, No. 8, pp. 2553-2580, Aug. 2010.

[6] A. Lesnicar and R. Marquardt, “An innovative modular multilevel converter topology suitable for a wide power range,” *in Proc. Power Tech Conference*, pp. 6, 2003.

[7] A. Alexander and M. Thathan, “Cell capacitor sizing in multilevel converters: cases of the modular multilevel converter and alternate arm converter,” *IET Renewable Power Generation*, Vol. 9, No. 1, pp. 78-88, Mar. 2015.

[8] A. J. Korn, D. M. Winkelnkemper, and D. P. Steimer, “Low output frequency operation of the modular multi-level converter,” *in Proc. IEEE Energy Convers. Congr. Expo.*, pp. 3993-3997, 2010.

[9] K. Ilves, A. Antonopoulos, L. Harnefors, S. Norrga, L. Angquist, and H. Nee, “Capacitor voltage ripple shaping in modular multilevel converters allowing for operating region extension,” *in Proc. Industrial Electronics, Control and Instrumentation*, pp. 4403-4408, 2011.

[10] S. Debnath and M. Saeedifard, “Optimal control of modular multilevel converters for low-speed operation of motor drives,” *in Proc. IEEE Applied Power Electronics Conf.*, pp. 247-254, 2014.

[11] J. Jung, H. Lee, and S. Sul, “Control strategy for improved dynamic performance of variable-speed drives with modular multilevel converter,” *IEEE J. Emerg. Sel. Topics Power Electron.*, Vol. 3, No. 2, pp. 371-380, Jun. 2015.

[12] A. Antonopoulos, L. Angquist, S. Norrga, K. Ilves, L. Harnefors, and H. Nee, “Modular multilevel converter ac motor drives with constant torque from zero to nominal speed,” *IEEE Trans. Ind. Appl.*, Vol. 50, No. 3, pp. 1982-1993, May/Jun. 2014.

[13] J. Kolb, F. Kammerer, M. Gommeringer, and M. Braun, “Cascaded control system of the modular multilevel converter for feeding variable-speed drives,” *IEEE Trans. Power Electron.*, Vol. 30, No. 1, pp. 349-357, Jan. 2015.

[14] M. Hagiwara, I. Hasegawa, and H. Akagi, “Start-up and low-speed operation of an electric motor driven by a

modular multilevel cascade inverter," *IEEE Trans. Ind. Appl.*, Vol. 49, No. 4, pp. 1556-1565, Jul./Aug. 2013.
[15] K. Wang, Y. Li, Z. Zheng, and L. Xu, "Voltage balancing and fluctuation-suppression methods of floating capacitors in a new modular multilevel converter," *IEEE Trans. Ind. Electron.*, Vol. 60, No. 5, pp. 1943-1954, May 2013.
[16] L. He, K. Zhang, J. Xiong, S. Fan, X. Chen, and Y. Xue, "New modular multilevel converter with power channels between upper- and lower arms suitable for MV drives," *in Proc. IEEE Applied Power Electronics Conf.*, pp. 799-805, 2015.
[17] B. Li, Y. Zhang, G. Wang, W. Sun, D. Xu, and W. Wang, "A modified modular multilevel converter with reduced capacitor voltage fluctuation," *IEEE Trans. Ind. Electron.*, Vol. 62, No. 10, pp. 6108-6119, Oct. 2015.
[18] T. Shimizu, Y. Jin, and G. Kimura, "DC ripple current reduction on a single-phase PWM voltage-source rectifier," *IEEE Trans. Ind. Appl.*, Vol. 36, No. 5, pp. 1419-1429, Sept./Oct. 2000.
[19] K. Tsuno, T. Shimizu, K. Wada, and K. Ishii, "Optimization of the DC ripple energy compensating circuit," *in Proc. Power Electronics Specialists Conference*, pp. 316-321, 2004.
[20] K. Chao, P. Cheng, and T. Shimizu, "New control methods for single phase PWM regenerative rectifier with power decoupling function," *in Proc. Power Electronics and Drive Systems*, pp. 1091-1096, 2009.
[21] R. Wang, F. Wang, D. Boroyevich, R. Burgos, R. Lai, P. Ning, and K. Rajashekara, "A high power density single-phase PWM rectifier with active ripple energy storage," *IEEE Trans. Power Electron.*, Vol. 26, No. 5, pp. 1430-1443, May 2011.
[22] H. Li, K. Zhang, H. Zhao, S. Fan, and J. Xiong, "Active power decoupling for high-power single-phase PWM rectifiers," *IEEE Trans. Power Electron.*, Vol. 28, No. 3, pp. 1308-1319, Mar. 2013.
[23] W. Qi, H. Wang, X. Tan, G. Wang, and K. D. T. Ngo, "A novel active power decoupling single-phase PWM rectifier topology," *in Proc. IEEE Applied Power Electronics Conf.*, pp. 89-95, 2014.
[24] Y. Tang, F. Blaabjerg, P. C. Loh, C. Jin, and P. Wang, "Decoupling of Fluctuating Power in Single-Phase Systems Through a Symmetrical Half-Bridge Circuit," *IEEE Trans. Power Electron.*, Vol. 30, No. 4, pp. 1855-1865, Apr. 2015.
[25] H. Zhao, H. Li, C. Min, and K. Zhang, "A modified single-phase h-bridge PWM rectifier with power decoupling," *in Proc. Industrial Electronics, Control and Instrumentation*, pp. 80-85, 2012.
[26] D. N. Zmood and D. G. Holmes, "Stationary frame current regulation of PWM inverters with zero steady-state error," *IEEE Trans. Power Electron.*, Vol. 18, No. 3, pp. 814-822, May 2003.
[27] S. Fan, K. Zhang, J. Xiong, and Y. Xue, "An improved control system for modular multilevel converters with new modulation strategy and voltage balancing control," *IEEE Trans. Power Electron.*, Vol. 30, No. 1, pp. 358-371, Jan. 2015.
[28] Q. Song, W. Liu, X. Li, H. Rao, S. Xu, and L. Li, "A steady-state analysis method for a modular multilevel converter," *IEEE Trans. Power Electron.*, Vol. 28, No. 8, pp. 3702-3713, Aug. 2013.
[29] D. Graovac and M. Pürschel, "IGBT power losses calculation using the datasheet parameters," Infineon Technol., Neubiberg, Germany, Appl. Note, vol. 1, Jan. pp. 1–17, 2009.
[30] Infineon FD400R33KL2C, [Online]. Available: http://www.infineon.com.

Xin Huang was born in Jiangsu, China, in 1989. He received his B.E. degree from the Huazhong University of Science and Technology (HUST), Wuhan, China in 2012. He is currently working toward his Ph.D. degree at the School of Electrical and Electronics Engineering, HUST, Wuhan, China. His research interests include design and control of power electronics systems, AC drives, and modular multilevel converters.

Kai Zhang received his B.S., M.S., and Ph.D. degrees from the Huazhong University of Science and Technology (HUST), Wuhan, China in 1993, 1996, and 2001, respectively. He joined HUST as an assistant lecturer in 1996 and was promoted to full-time professor in 2006. He was a visiting scholar at the University of New Brunswick, Fredericton, NB, Canada from 2004 to 2005. He is the author of more than 60 technical papers. His current research interests include uninterruptible power systems, railway traction drives, modular multilevel converters, and electromagnetic compatibility techniques for power electronic systems.

Jingbo Kan was born in Shandong Province, China. He received his B.E. degree from the Shandong University, Jinan, China in 2004 and his M.E. degree from Anhui University of Technology, Maanshan, China in 2009. He is currently working toward his Ph.D. degree at the School of Electrical and Electronics Engineering, Huazhong University of Science and Technology, Wuhan, China. His research interests include railway traction drives and optimized pulse–width modulation techniques.

Jian Xiong received his B.S. degree from the East China Shipbuilding Institute, Zhenjiang, China in 1993 and his M.S. and Ph.D. degrees from the Huazhong University of Science and Technology (HUST), Wuhan, China in 1996 and 1999, respectively. He joined HUST as a lecturer in 1999 and became an associate professor in 2003. His current research interests include uninterruptible power systems, AC drives, switch-mode rectifiers, STATCOMs, and their related control techniques.